Applied Catalysis B: Environmental 305 (2022) 121045

Contents lists available at ScienceDirect

Applied Catalysis B: Environmental

journal homepage: www.elsevier.com/locate/apcatb

Photovoltaic powered solar hydrogen production coupled with waste SO_2 valorization enabled by MoP electrocatalysts

Jaemin Park [a], Hyunseok Yoon [b], Dong-Yeop Lee [b], Su Geun Ji [c], Wooseok Yang [d], S. David Tilley [d], Myeong-Chang Sung [b], Ik Jae Park [e], Jeiwan Tan [a], Hyungsoo Lee [a], Jin Young Kim [c,f,*], Dong-Wan Kim [b,*], Jooho Moon [a,*]

[a] Department of Materials Science and Engineering, Yonsei University, Seoul 03722, Republic of Korea
[b] School of Civil, Environmental and Architectural Engineering, Korea University, Seoul 02841, Republic of Korea
[c] Department of Materials Science and Engineering, Seoul National University, Seoul 08826, Republic of Korea
[d] Department of Chemistry, University of Zurich, Zurich 8057, Switzerland
[e] Department of Applied Physics, Sookmyung Women's University, Seoul 04310, Republic of Korea
[f] Research Institute of Advanced Materials (RIAM), Institute of Engineering Research, Seoul National University, Seoul 08826, Republic of Korea

ARTICLE INFO

Keywords:
Water splitting
Solar hydrogen
Molybdenum phosphide
Sulfite oxidation reaction
Tandem photovoltaics

ABSTRACT

In this study, we demonstrated high-rate H_2 generation by coupling with the sulfite oxidation reaction (SOR) as an alternative to the oxygen evolution reaction for solar H_2 production. The emerging and cost-effective molybdenum phosphide electrocatalyst was appropriately optimized and used as a bifunctional catalyst in an alkaline electrolyte for both SOR and HER. Powered by state-of-the-art perovskite–Si tandem photovoltaics, a remarkable photocurrent density of over 17 mA cm^{-2} was achieved in the HER coupled with the SOR. In addition to the significantly enhanced photocurrent, the SOR can further reduce the overall cost of solar H_2 production owing to the elimination of the expensive membranes required for H_2 and O_2 gas separation. Considering the high global demand for desulfurization via the SOR, the strategy proposed here will enable practical H_2 production from renewable sources while effectively converting the toxic SO_2 gas into a value-added product for the chemical industry.

1. Introduction

Despite the growth in renewable energy sources over the past few decades, fossil fuels continue to be the dominant energy sources worldwide. Their use for electricity generation, e.g., continued to rise to 68% of the worldwide electricity in 2017 [1]. Although fossil fuel power plants can generate reliable electricity at low prices, carbon-based fuels inevitably produce large amounts of carbon dioxide (CO_2) and sulfur dioxide (SO_2) gases, which induce irrecoverable climate change and atmospheric pollution [2]. In comparison, hydrogen (H_2) is a storable clean chemical fuel that does not emit CO_2 and SO_2 during combustion. However, because 95% of the H_2 produced currently originates from fossil fuels (i.e., gray H_2), the H_2 production process still produces CO_2 as a by-product [3]. In this regard, H_2 generation by solar water splitting ($2H_2O \longrightarrow 2H_2 + O_2$) is recognized as one of the simplest solutions for producing clean H_2 without generating harmful by-products [4].

Despite its promising concept, the typical solar water splitting system faces a fundamental challenge for practical H_2 generation owing to the high potential energy required to drive the H_2 evolution reaction (HER) with the oxygen evolution reaction (OER). Specifically, a potential of 1.23 V is required to provide the thermodynamic driving force along with a potential of approximately 0.5 V for the overpotential associated with the reaction kinetics [5]. The OER significantly limits the overall reaction owing to its sluggish kinetics and four-electron transfer step [6]. Moreover, not only is generating oxygen unnecessary particularly because of its abundance but also becomes of the explosive nature of its mixture with H_2. Thus, an additional gas separation infrastructure is necessary to prevent gas accumulation, thereby raising the initial capital cost [7]. Thus, many studies have explored alternative reactions to the OER [8–10]. However, there are few reactions that satisfy all requirements for an ideal alternative, including a low thermodynamic energy requirement when coupled with the HER as well as a global

* Corresponding author at: Department of Materials Science and Engineering, Seoul National University, Seoul 08826, Republic of Korea.
* Corresponding authors.
E-mail addresses: jykim.mse@snu.ac.kr (J.Y. Kim), dwkim1@korea.ac.kr (D.-W. Kim), jmoon@yonsei.ac.kr (J. Moon).

https://doi.org/10.1016/j.apcatb.2021.121045
Received 25 August 2021; Received in revised form 10 December 2021; Accepted 23 December 2021
Available online 28 December 2021
0926-3373/

demand commensurate with the scale of global H_2 production, which is mainly used in the chemical industry.

The sulfite oxidation reaction (SOR) can potentially meet these requirements. The standard electrode potential of the SOR under alkaline conditions (Eq. (1)) does not require any thermodynamic energy input when coupled with the HER (Eq. (2)) and must only overcome the kinetic barrier (Eq. (3)) [11].

$$SO_4^{2-} + H_2O + 2e^- \rightarrow SO_3^{2-} + 2OH^- \quad E_{red}^0 = -0.93 \text{ V vs. NHE} \tag{1}$$

$$2\,H_2O + 2e^- \rightarrow H_2 + 2OH^- \quad E_{red}^0 = -0.83 \text{ V vs. NHE} \tag{2}$$

$$SO_3^{2-} + H_2O \rightarrow SO_4^{2-} + H_2 \quad E_{cell} = +0{\cdot}10 \text{ V} \tag{3}$$

The SOR can be used for the desulfurization of sulfur dioxide (SO_2) in the form of flue gas, which is typically produced during the combustion and extraction of sulfur-containing fossil fuels. SO_2 emissions cause a broad range of environmental issues related to agriculture and climate (e.g., acid rain) and even threaten human health [12]. Most fossil fuel-based power plants and oil refineries have been controlled at ultra-low emission levels of SO_2 (i.e., 35 mg Nm^{-3}) to meet the strict environmental protection standard for utilizing flue gas desulfurization (FGD) technology [13]. Accordingly, the market size of the global FGD reached USD 25.1 billion in 2019 and is expected to grow owing to the massive SO_2 emissions [14]. Among the conventional FDG technologies, including magnesium-enhanced lime, dual alkali, and ammonia-based methods, limestone–gypsum wet desulfurization is the most commonly used because of its low removal cost [15]. However, the limestone used in the process leads to not only release CO_2, but also leave behind gypsum ($CaSO_4$), which is now considered to pose a new environmental issue [16].

Another typical treatment involves using aqueous sodium hydroxide (NaOH) solution to absorb SO_2 [17]. In the absence of CO_2 emission and gypsum formation, an aqueous solution of Na_2SO_3 is produced as a by-product. After SO_2 absorption, the solution is purged with air to oxidize into Na_2SO_4 because not only it is a chemically inert and nontoxic compound but can also be used in the paper industry, glass production, and various other applications [17]. However, this additional aeration process costs some energy and simultaneously causes loss of the potential energy in SO_3^{2-}. If the SOR can be integrated with solar H_2 generation, substantial economic benefits can be expected. The integration of solar-powered H_2 production and sulfite oxidation with natural gas refinery plants requiring massive sulfur recovery can become an excellent solution. Although H_2 production by the photoelectrochemical oxidation of SO_3^{2-} using $BiVO_4$ photoanodes has been demonstrated, [18,19] H_2 could not be generated under unbiased conditions. Moreover, the resulting H_2 production current density is orders of magnitude lower than the practical solar H_2 conversion benchmark of 10 mA cm^{-2} owing to the lack of an optimal SOR catalyst. HER and SOR experiments should be performed in an alkaline electrolyte because, in an acid electrolyte, disproportionation of HSO_3^- to elemental sulfur and SO_4^{2-} occurs instead of H_2 production [11]. Thus, developing a highly active bifunctional electrocatalyst for the HER and the SOR in alkaline electrolytes is essential for efficient H_2 production.

Molybdenum phosphide (MoP) is the best choice as a highly active bifunctional electrocatalyst in a basic electrolyte. MoP has been extensively investigated as a promising candidate for substituting commercial Pt-based electrocatalysts owing to its low cost, suitable electronic structure (Pt-like) for the HER, good electrical conductivity, and even high chemical stability over a wide pH range [20–22]. Even in alkaline media, most MoP catalysts exhibit long-term stability without severe deterioration, unlike other metal phosphides [23,24]. To enhance the electrocatalytic performance of MoP, various synthetic strategies were explored. For example, nanostructuring can enlarge the exposed active surface area, [25,26] and designing binder-free electrodes can be further beneficial for reducing the "dead volume" and ensuring rapid charge transfer between the catalytic material and the conductive substrate [27,28]. Moreover, fabrication of bimetallic or multimetallic hybrid catalysts by doping or alloying can optimize their electronic structure toward a specific electrochemical reaction [29,30]. Hence, developing MoP-based materials with outstanding electrocatalytic properties for the HER as well as presenting excellent performance for the SOR will significantly contribute to achieving cost-effective and efficient H_2 production.

Herein, we present an unassisted H_2 generation system employing the SOR as an alternative anodic reaction. MoP-based electrodes were carefully optimized to reveal the high catalytic activities for both HER and SOR in alkaline electrolytes. It was shown that depositing a small amount of Pt on the MoP-based electrodes causes the activity of MoP for the HER to exceed that of commercial Pt/C catalyst in a basic electrolyte. To supply the required energy to drive the HER and the SOR, we employed state-of-the art tandem photovoltaics (PVs), which utilizes a wide-bandgap perovskite (~ 1.7 eV)–Si tandem configuration with a maximum power conversion efficiency (*PCE*) of 26.6%. Combined with the highly efficient bifunctional electrocatalyst and PV, the PV-powered H_2 evolution system coupled with the SOR demonstrates a remarkable H_2 generation photocurrent density of over 17 mA cm^{-2} under 1-sun illumination. It corresponds to 21% solar-to-hydrogen conversion efficiency in a traditional water splitting cell (*HER+OER*), with a prolonged durability of up to 80 h. Our approach not only enables simultaneous SO_2 removal and enhanced H_2 generation but also eliminates the use of expensive gas-separation membranes because the OER is replaced by the SOR without evolved gas.

2. Experimental section

2.1. Materials

MoO_2 powder was synthesized using the electrical explosion method with a Mo wire (Nano Technology Inc.) using an electrical pulse equipment (NTi-10 C, Nano Technology Inc.). $H_2PtCl_6{\cdot}6H_2O$, poly(triaryl amine) (PTAA), toluene, cesium iodide (CsI), lead bromide ($PbBr_2$), lead thiocyanate ($Pb(SCN)_2$), N,N-dimethylformamide (DMF), 1-methyl-2-pyrrolidinone (NMP), polyethyleneimine (PEIE), 5 wt% Nafion solution, and methanol were purchased from Sigma Aldrich (St. Louis, MO, USA). $NaH_2PO_2.2\,H_2O$, formamidinium iodide (FAI), methylammonium bromide (MABr), and phenethylammonium (PEAI) were purchased from Greatcell Solar (Queanbeyan, Australia). Lead iodide (PbI_2), and Pt/C (20 wt% Pt) was purchased from Alfa Aesar (Ward Hill, MA, USA). Diethyl ether (DE) was purchased from Daejung. C_{60} was purchased from Nano-c (Westwood, MA, USA).

2.2. Synthesis of MoP/porous carbon cloth (PCC)

MoP/PCC was synthesized by the thermal phosphidation process using MoO_2/PCC, which was fabricated as described in our previous report [27]. MoO_2/PCC and $NaH_2PO_2{\cdot}2H_2O$ (2 g) were placed in the heat zone area and upstream zone of a tube furnace, respectively. The samples were heated at 400 °C for 2 h under flowing Ar/H_2 (5%) gas. After 2 h, the temperature was raised to 600 °C, and the quartz tube was moved to place $NaH_2PO_2{\cdot}2H_2O$ into the heat zone, to generate PH_3 gas, and held for 2 h.

2.3. Pt coating on Pt^x/MoP/PCC ($x = 1, 2$) and Pt/PCC

Pt decoration on MoP/PCC is considered as an aerobic alcohol oxidation process [31]. 5 pieces of MoP/PCC were placed in a three-neck, round- bottom flask with 60 mL of absolute ethanol. Absolute ethanol solution (2.54 mL) that dissolved H_2PtCl_6 (52.8 mg, Sigma Aldrich) was added to the flask and refluxed at 70 °C for 2 h. After 2 h, 0.2 M NaOH (1.27 mL) solution was added to the flask and refluxed additionally for 0.5 h to reduce the residue. After the reaction, the substrate was washed and dried in an electrical oven. The Pt/PCC

electrode was prepared using the same Pt decoration process with a bare PCC substrate.

2.4. Fabrication of monolithic perovskite–Si tandem solar cells

For the fabrication of perovskite–Si tandem solar cells, perovskite top cells were stacked on a Si heterojunction with an intrinsic thin-layer (HIT) solar cell as previously described [32]. Rear-side-textured 250 μm-thick n-type Si wafers prepared by the floating zone technique were used for the bottom cell. Approximately 10–20 nm-thick n- and p-doped amorphous Si (a-Si) thin films were deposited on the front and rear sides of a Si wafer, respectively. Approximately 80 nm-thick ITO and 500 nm-thick Ag layers were deposited on the rear side for electrical contact, whereas a 20 nm-thick ITO layer was employed on the front side as a recombination layer between the subcells. Each perovskite top cell was fabricated in a N_2-filled glove box. A PTAA solution (5 mg/mL in toluene) was spin-coated at 6000 rpm onto the recombination layer and annealed at 100 °C for 10 min. Stoichiometric $FA_{0.70}MA_{0.15}Cs_{0.15}Pb(I_{0.85}Br_{0.15})_3$ salts with 1 mol% PEAI and 2 mol% $Pb(SCN)_2$ additives were dissolved in the DMF and NMP mixed solvent (4:1 vol ratio) with 1.2 M perovskite precursor solution. Perovskite layers were deposited by spin-coating at 3000 rpm and immersed in DE for 30 s. After DE bathing, the film was annealed for 10 min at 100 °C. As an electron-selective layer, a 20 nm-thick C_{60} layer was deposited by thermal evaporation. Subsequently, 0.2 wt% PEIE solution in methanol was spin-coated at 6000 rpm, and 40 nm-thick ITO and 500 nm-thick Ag layers were formed by the same method as that used for the rear-contact.

2.5. Characterizations of catalyst material

X-ray diffraction (XRD) patterns were obtained with a Rigaku MiniFlex 600 diffractometer using Cu Kα radiation. TEM analysis with EDS mapping was conducted using a JEOL JEM-2100 F instrument. Surface chemical analysis was performed by XPS measurements using a K-alpha+ equipment. The elemental composition of each catalyst was determined by ICP-AES (Jobin Yvon Ultima 2). HPLC (1260 Infinity, Agilent, USA) was performed to evaluate the concentrations of SO_3^{2-}/SO_4^{2-} in the electrolyte.

2.6. Electrocatalytic performance evaluation of catalyst

Current density–voltage (J–V) curves of the PV were acquired under simulated AM 1.5 G illumination (100 mW cm^{-2}, Oriel Sol3A Class AAA Solar Simulator, Newport). Electrochemical measurements were performed with conventional two-electrode and three-electrode configurations using a potentiostat (SI 1287, Solartron, Leicester, UK). An Ag/AgCl/KCl (saturated) electrode was used as the reference, while either a coiled Pt wire or graphite rod was used as counter electrode. The catalytic performances for all the cathodes were evaluated within the initial 5 cycles in our study. The scan rate for the J–V curves was 5 mV s^{-1}. All potentials were corrected with iR compensation to remove the ohmic potential and converted to the RHE. EIS measurements were performed at a frequency ranging from 100 kHz to 10 mHz at open circuit voltage using a potentiostat (1287 A, Solartron). For comparison, commercial Pt/C HER catalyst was utilized. PCC was coated with the Pt/C ink. The ink was prepared by dispersing Pt/C (20 wt% Pt) powder (10 mg) in water/IPA solution (750/200 μL) and 5 wt% Nafion solution (50 μL), followed by ultrasonication for 30 min. This catalyst ink (50 μL) was then dropped onto the PCC, followed by drying. Gas chromatography (GC, 6500GC system, YL Instruments, Korea) was conducted for gas-product analysis. EIS was performed during chronoamperometry measurements in the frequency range of 300 kHz–1 Hz at 1.25 V vs. RHE with an AC amplitude of 10 mV.

2.7. PV-electrolysis tandem cell assembly and H_2 generation

During the overall photoassisted electrolysis, the perovskite–Si PV was connected with wires to catalyst electrodes immersed in an electrolyte, while simulated 1 sun light (AM 1.5G) was irradiated to the PV. The electron and hole collectors of the PV were connected to cathode and anode, respectively; therefore, the electrons were moved to cathode where HER occurs, whereas the holes were transferred to anode where SOR occurs. A Si diode (Newport Corporation) was used for calibrating the light intensity so as to locate the PV at the position corresponding to the 1 sun level. The scan rate for the J–V curves was 10 mV s^{-1}. PV cell was in contact with a temperature-controlled stage (LTS420E-PB4, Linkam, USA) under N_2 atmosphere during stability test. The surface temperature of the PV was maintained at 15 °C when illuminated with 1 sun light.

3. Results and discussion

3.1. Catalyst preparation and characterization

The MoP electrode was prepared by dip-coating into an-electrically exploded MoO_2 precursor solution, followed by thermal phosphidation. Porous carbon cloth (PCC) was chosen as a substrate because of its high electrical conductivity and porous microstructure for maximizing the contact area between the catalytic material and the conductive substrate (Fig. S1) [27]. The resulting MoP electrode (denoted as MoP/PCC) was further decorated with Pt by the ethanol oxidation method (denoted as Pt^x/MoP/PCC (x = 1,2), where x depends on the amount of decorated Pt, see the Experimental Section for details). Pt/PCC was also prepared as a reference electrode using the same Pt deposition process with a bare PCC substrate. The corresponding X-ray diffraction (XRD) patterns are shown in Fig. 1a. All samples showed a broad peak of graphitic carbon at 2θ~26°, which was attributed to the PCC substrate. All the reflected peaks in the XRD pattern of MoP/PCC agreed well with those in the MoP reference data (#24-0771). After incorporation with Pt, no phase change was observed in Pt^x/MoP/PCC as compared with MoP/PCC; however, the characteristic peaks of metallic Pt were discernable, whose intensities varied in proportion to the amount of dissolved Pt during the deposition. Accurate elemental weight ratios of Mo, P, and Pt in each Pt^x/MoP/PCC were measured via inductively coupled plasma atomic emission spectroscopy (ICP-AES) analysis (Table S1). The decorated Pt amounts were 4.88 wt% and 22.08 wt% for Pt^1/MoP/PCC and Pt^2/MoP/PCC, respectively.

The microstructural and crystalline information of MoP/PCC and Pt^x/MoP/PCC were obtained via Transmission electron microscopy (TEM) analysis (Fig. 1b–f). Fig. 1b shows a low-magnification TEM image of MoP/PCC, indicating that the average size of the MoP particles is 40–50 nm. The selected area electron diffraction (SAED) pattern with well-defined ring patterns corresponding to the (001), (100), (101), and (110) planes of MoP indicates that MoP/PCC has a polycrystalline structure (Fig. 1c). The HRTEM images of Pt^1/MoP/PCC and MoP/PCC show that Pt nanoparticles with diameters of 2–3 nm were attached as dots on the surface of MoP particles, although the overall morphology was unchanged after Pt loading (Fig. 1d and Fig. S2). Moreover, the lattice spacing of 0.226 nm in the attached particles matches well with the (111) plane of cubic Pt (Fig. 1e). The electron dispersive X-ray spectroscopy (EDS) mapping with TEM analysis demonstrates that each Pt nanoparticle is decorated on the surface of the MoP particles (Fig. 1f).

The surface structure and chemical states of MoP/PCC and Pt^1/MoP/PCC were comparatively analyzed by X-ray photoelectron spectroscopy (XPS) analysis (Fig. 1g–i). Fig. 1g presents the high-resolution Mo 3d spectra. For MoP/PCC, the two pairs of deconvoluted peaks at 236.2/233.4 eV and 232.9/229.2 eV are attributed to Mo^{6+} $3d_{3/2}/3d_{5/2}$ and Mo^{4+} $3d_{3/2}/3d_{5/2}$, respectively, from the high oxidation state of MoO_x formed on the surface of MoP [20,33]. Fig. 1h shows the high-resolution P 2p spectra in which the peaks at 134.2 eV are consistent with P–O

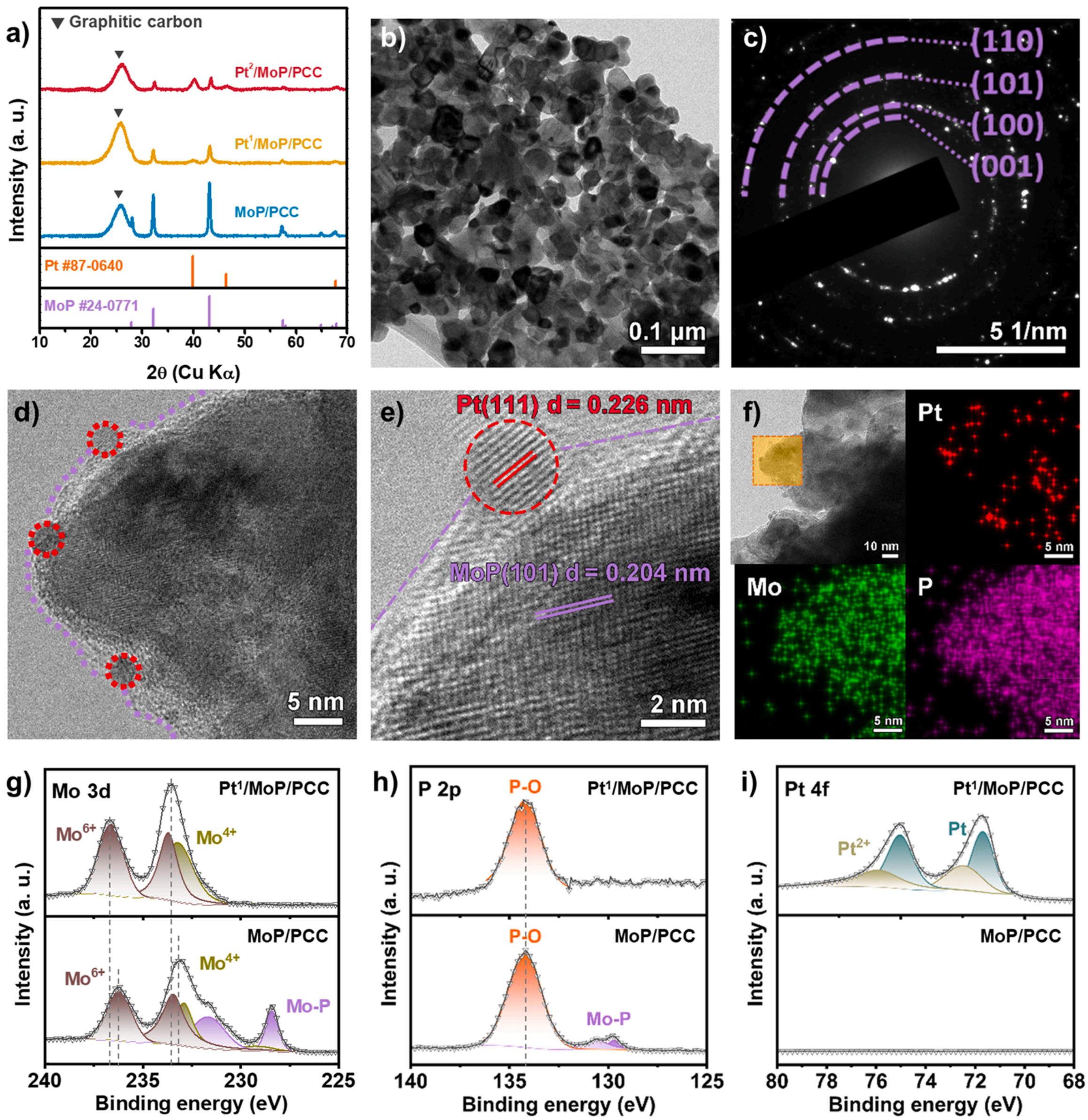

Fig. 1. a) XRD patterns of MoP/PCC and Pt^x/MoP/PCC (x = 1, 2). b) Low-magnification TEM image and c) SAED patterns of MoP/PCC. d, e) HRTEM images and f) TEM-EDS mapping of Pt^1/MoP/PCC. g) Mo 3d, h) P 2p, and i) Pt 4f XPS spectra of MoP/PCC and Pt^1/MoP/PCC.

binding [34,35]. The characteristic peaks at 231.7/228.4 eV for Mo 3d and at 130.6/129.7 eV for P 2p represent Mo–P binding, which is in good agreement with a previously reported MoP structure (Fig. 1g, h) [20,33–35]. These Mo-P peaks (purple color) disappear after Pt incorporation in both Mo 3d and P 2p spectra. During the Pt decoration process including washing with deionized water and thermal treatment, the surface of MoP was exposed to air, so that the Mo–P peaks in the Mo 3d and P 2p spectra were transformed to Mo–O and phosphate [20]. The O 1s valence band spectra of MoP/PCC is deconvoluted to two peaks at 531.59 eV and 533.02 eV, which are attributed to lattice oxygen (O_L), oxygen deficient regions (O_V), respectively (Fig. S3) [36]. The decreased content of O_V components was displayed in Pt^1/MoP/PCC, which resulted from the surface oxidation of MoP/PCC during the Pt deposition [36]. The Pt 4f spectrum is deconvoluted to two pairs of peaks at 75.9/72.4 (Pt^{2+}) and 75/71.7 eV (metallic Pt), which are only observed for Pt^1/MoP/PCC (Fig. 1i) [31]. Interestingly, the Mo 3d peaks in Pt^1/MoP/PCC and Pt 4f peaks in Pt/PCC are slightly shifted to higher and lower binding energies, respectively, whereas there are no evident chemical shifts in the P 2p spectra compared to MoP/PCC (Fig. 1g, h and Fig. S4). It should be noted that O_L peak slightly shifted to lower binding energies (Fig. S3). Therefore, there is no electronic interaction between Pt and O as both Pt 4f and O 1s peaks shift to lower binding energies after Pt deposition. It is well known that the coupling of transition metal-based compounds with Pt leads to tuning of the electronic structures, and the chemical shifts of the Mo 3d spectra indicate that electronic interactions exist primarily between Mo and Pt in this system [37–39]. It should be noted that Pt has stronger electronegativity compared to Mo atom. Therefore, it is speculated that partial electron transfer from Mo to Pt occurs through the electronic interactions, which is expected to tightly bind between Mo and Pt and facilitate electron transfer during the catalytic reaction [39].

3.2. *Catalytic performance of MoP based electrode toward SOR*

Fig. 2a displays the advantage of the SOR compared to the OER when coupled with the HER. In the absence of Na_2SO_3, the half-cell reaction at the anode is.

$$2H_2O + O_2 + 4\ e^- \rightarrow 4\ OH^- \quad E_{red}^0 = 0.401\ V\ vs.\ NHE \tag{4}$$

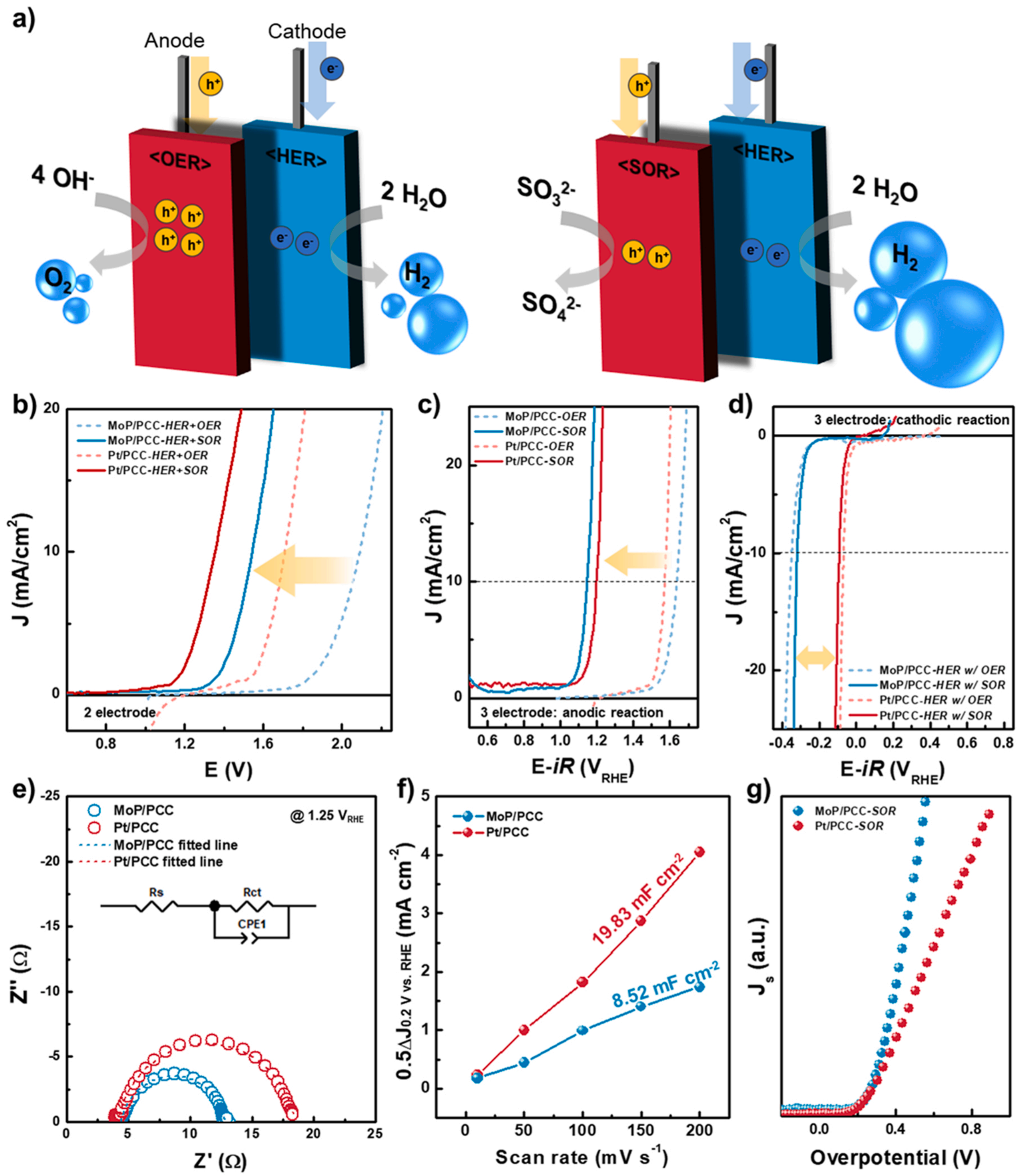

Fig. 2. a) Conceptual diagram of hydrogen production system using SOR instead of OER. b) J–V curve of MoP/PCC and Pt/PCC electrodes in two-electrode configuration. J–V curves of MoP/PCC and Pt/PCC electrodes with or without Na_2SO_3 for c) anodic and d) cathodic reaction in three-electrode configuration. e) Nyquist plots obtained from EIS measurements conducted at 1.25 V vs. RHE. Scatter points represent original experimental data, whereas dotted lines denote fitted curves based on equivalent circuit shown in inset. f) Capacitive current densities as function of scan rate. Slope represents C_{dl}. g) J–V curves with ECSA-normalized current density.

Therefore, the overall reaction requires approximately 1.23 V as the minimum thermodynamic energy. In contrast, when SO_3^{2-} is added as a reactant for the oxidation reaction, the thermodynamic requirement reduces owing to the two-electron transfer (Eqs. (1)–(3)). The electrolyte composition was optimized (Fig. S5 and Supplementary Note 1). In Fig. 2b, the electrocatalytic properties of the MoP/PCC and Pt/PCC electrodes are presented when the HER is coordinated with either the OER or the SOR (i.e., denoted as *HER+OER* and *HER+SOR*, respectively) in a two-electrode configuration. Both electrodes exhibited a similar phenomenon; however, a negative shift in the onset potential was observed when the OER was replaced by the SOR. The Pt/PCC and MoP/PCC electrodes for *HER+OER* showed the potential onsets of 1.53 and 1.8 V and of 1.13 and 1.34 V for *HER+SOR*, respectively.

The differences in the electrocatalytic activities of both electrodes toward HER and OER/SOR were investigated using a conventional three-electrode configuration to distinguish the separated electrocatalytic activity between HER and OER/SOR. An earlier onset potential was observed in the anodic reaction side as expected when the OER was replaced by the SOR (Fig. 2c), whereas the HER remained almost identical regardless of the presence of SO_3^{2-} (Fig. 2d). This indicates that the reduced energy requirement for the anodic reaction is mainly attributed to the shift in the onset potential in the two-electrode

configuration. Noticeably, MoP/PCC showed superior electrocatalytic performance for the SOR, even higher than that of Pt/PCC, whereas it presented a lower catalytic activity toward the OER than Pt/PCC (Fig. 2c). Electrochemical impedance spectroscopy (EIS) was conducted for MoP/PCC and Pt/PCC at 1.25 V vs. RHE in a three-electrode configuration in the presence of SO_3^{2-} (Fig. 2e). An equivalent circuit model consisting of one series resistance (R_s), a parallel pair of resistance (R_{ct}), and a constant-phase element (CPE1) was employed for fitting the EIS data (inset of Fig. 2e). All EIS plots consist of a single semicircle at low frequencies (approximately 10–10^3 Hz), which is related to the charge transfer resistance (R_{ct}) representing the electrocatalytic kinetics [40]. The fitted results revealed that MoP/PCC had a lower R_{ct} value than Pt/PCC (Table S2) in the presence of SO_3^{2-}, which is indicative of a more rapid charge transfer kinetics than that of MoP/PCC. The specific activity (referred to as the specific current density per catalyst surface area, J_s) is an activity metric to compare the intrinsic activity of catalysts having different surface areas or loadings [41]. According to Eqs. (5) and (6), J_s is determined by the current density per geometric active area (J_g) and the electrochemical active area (ECSA), which is proportional to the double-layer capacitance (C_{dl}) [41].

$$J_S = \frac{J_g \times A}{ESCA} \tag{5}$$

$$ECSA = \frac{C_{dl}}{C_s} \tag{6}$$

where A is the geometric active area and C_s is the specific capacitance, which is identical for both catalysts because of the same electrolyte system used. C_{dl} can be extracted by performing cyclic voltammetry (CV) at multiple scan rates under the potential region that does not contain electrochemical potentials of oxidation/reduction. The measured C_{dl} of Pt/PCC (19.83 mF cm^{-2}) was higher than that of MoP/PCC (8.52 mF cm^{-2}), suggesting a larger ECSA of Pt/PCC (Fig. 2f). As normalized by the ECSA, J_s for the SOR was evaluated as a function of the applied overpotential (Fig. 2g). A lower potential was required for MoP/PCC than that for Pt/PCC to achieve the same current density. This trend became more apparent at a higher current density, clearly suggesting that MoP/PCC has a higher intrinsic catalytic activity toward the SOR than Pt/PCC. A commercially available dimensionally stable anode (DSA, Ir- and Ru-coated Ti plate) was utilized as a reference electrode, which is known as an active OER catalyst. As expected, MoP/PCC showed inferior activity toward OER than DSA. In contrast, MoP/PCC revealed even slightly higher SOR catalytic performance than DSA (Fig. S6). Although both SOR and OER belong to anodic oxidation reaction, different catalytic activity between OER and SOR could be observed over MoP/PCC, while highlighting the excellent catalytic activity of MoP/PCC toward SOR. This result also clearly indicates that the necessity to use expensive noble metal-based OER catalysts can be relieved when the SOR is coupled with HER. However, MoP/PCC demonstrated a lower HER performance than Pt/PCC (Fig. 2d), resulting in inferior onset potential when they were evaluated in a two-electrode configuration (Fig. 2a). Consequently, this suggests that MoP requires

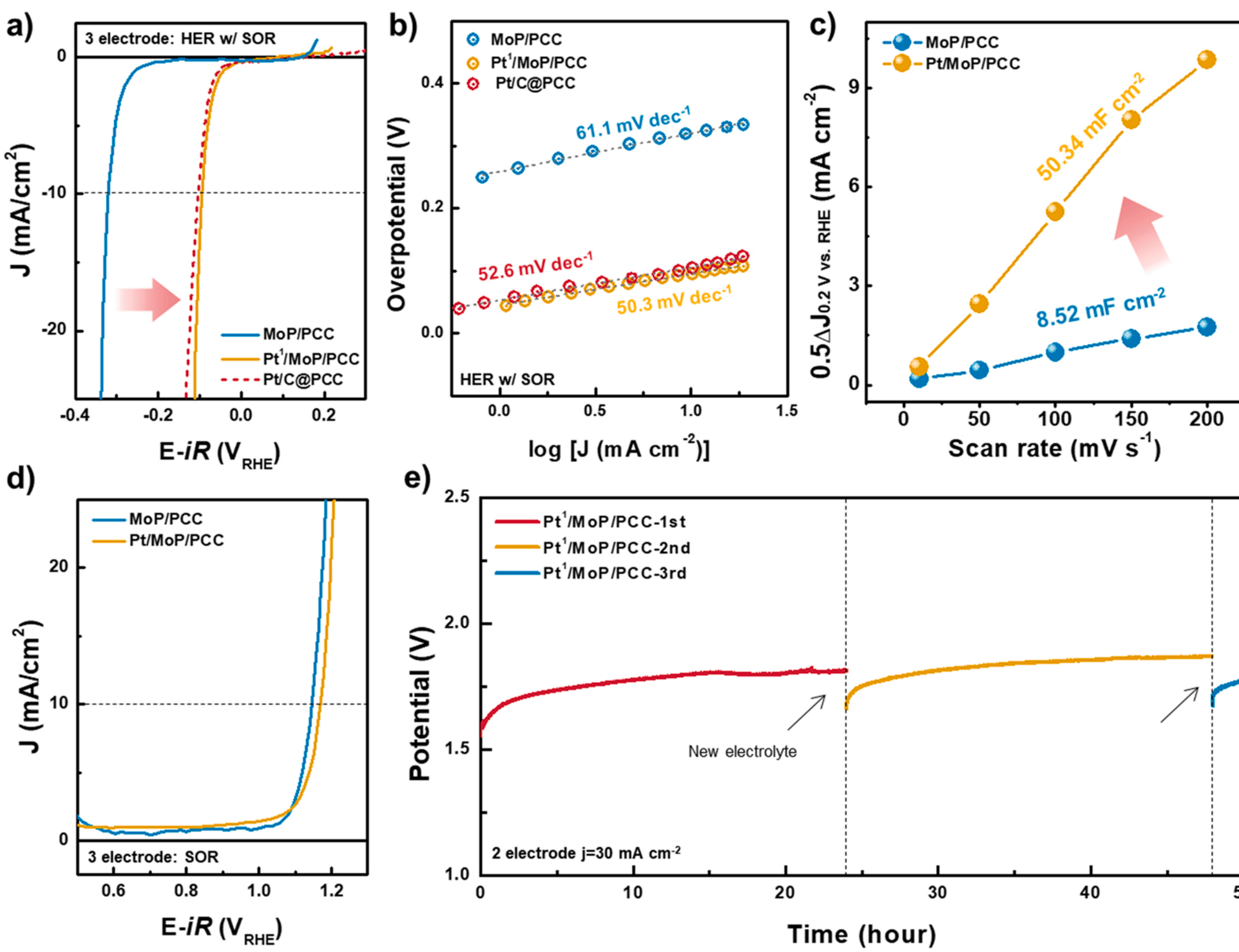

Fig. 3. Electrocatalytic performance of MoP/PCC, Pt^1/MoP/PCC, and Pt/C in *Na_2SO_3 (0.25)* electrolyte. J–V curve for a) HER, b) corresponding Tafel plots. c) Capacitive current densities as function of scan rate. Slope represents C_{dl}. d) J–V curve for HER in a three-electrode configuration. e) Chronopotentiometric test of Pt^1/MoP/PCC electrode at constant current density of 30 mA cm^{-2} in a two-electrode configuration.

further improvement on the electrocatalytic activity toward HER for high rate H_2 generation.

To further enhance the electrocatalytic HER performance, a small amount of Pt was decorated on the surface of MoP/PCC. The HER electrocatalytic performance of MoP decorated with Pt nanoparticles was investigated, along with the performance of the commercial Pt (20%)/C catalyst for comparison as shown in Fig. 3a, b. The HER performance was measured in a three-electrode configuration. The HER catalytic activity of Pt^1/MoP/PCC was enhanced, requiring only 89 mV of overpotential to deliver a current density of 10 mA cm^{-2}, and its Tafel slope was estimated to be 50.3 mV dec^{-1}. The higher exchange current density and lower Tafel slope associated with Pt^1/MoP/PCC compared to MoP/PCC clearly reveal Pt-induced catalytic activity improvement. It is known that Pt counter electrode can be dissolved and re-deposited on working electrode when HER performance is measured under three-electrode configuration. However, as shown in Fig. S7, we observed the identical HER performance of Pt^1/MoP/PCC under three-electrode configuration using either Pt or graphite counter electrode, indicating that there was no dissolution/re-deposition of Pt counter electrode. As shown in Fig. 3c, the larger C_{dl} of Pt^1/MoP/PCC (50.34 mF cm^{-2}) compared with MoP/PCC was calculated from continuous CV (Fig. S8). This confirms that the electronic interaction between Mo and Pt found in XPS analysis increases ECSA and facilitates HER. As shown in Fig. S9, nearly identical HER performance was observed for all three electrodes, indicating that no further enhancement of activity was observed with the increasing amount of deposited Pt. Moreover, depositing more than 22.08 wt% of Pt (Pt^2/MoP/PCC) is not only economically unrealistic, but also causing the agglomeration of Pt. This suggests that only 4.88 wt % Pt loading maximizes HER activity, while ensuring the cost-effectiveness. Moreover, Pt^1/MoP/PCC demonstrated outstanding HER performance in acidic electrolyte without Na_2SO_3, requiring only 37 mV of overpotential to deliver a current density of 10 mA cm^{-2}, and its Tafel slope was estimated to be 28.8 mV dec^{-1} (Fig. S10). The superior catalytic activity compared to non-Pt metal-based catalysts suggested that the small amount of Pt deposition is essential for the high rate H_2 generation in our system (Table S3).

Water splitting is considered to proceed by two steps: 1) the Volmer step and 2) the Heyrovsky or Tafel step [42]. In the first step, a proton is captured by the electron transfer from the cathode, forming an adsorbed hydrogen (H_{ad}) intermediate state on the active site of the catalyst surface. The second step involves H_{ad} coupling with either a new electron and another proton (Heyrovsky) or another H_{ad} (Tafel) to form H_2. In general, the HER activities of catalysts in an alkaline medium are lower than those in an acidic medium because an additional water dissociation process ($H_2O \rightarrow H^+ + OH^-$) is required in the Volmer reaction step in the former [42]. Thus, despite its excellent capability to convert the H_{ad} intermediate into hydrogen, Pt presents a lower activity in an alkaline electrolyte than that in an acidic one owing to the inefficient ability of water dissociation [42]. It is found that developing hybrid catalysts incorporating both Pt and the active component for water dissociation can increase the HER activity in alkaline electrolytes. In MoP, electron density is transferred from a metal to a phosphorous atom in transition metal phosphides because of the high electronegativity of phosphorus [43]. This indicates that phosphorus and metal atoms function as proton- and hydride-acceptors, respectively; thus, providing more active sites and facilitating the cleavage of the HO–H bond. Therefore, by depositing Pt on MoP, it is possible to produce a desirable catalyst for the dissociation of water as well as the H_2 conversion of H_{ad}. Accordingly, the combination of MoP and Pt increased the electrocatalytic activity for HER, resulting in a better catalytic activity than even commercial Pt/C in an alkaline electrolyte containing Na_2SO_3 (Fig. 3a). Interestingly, no significant difference was noted in the SOR catalytic activities of the MoP/PCC and Pt^1/MoP/PCC electrodes, regardless of the presence of Pt (Fig. 3d). It should be noted here that the overall system cost could be reduced by selecting a MoP/PCC electrode as the anode instead of Pt^1/MoP/PCC owing to the exclusion of expensive Pt. Catalyst stability is also essential for practical H_2 production. To assess the durability of the Pt^1/MoP/PCC electrode, chronopotentiometric tests at a current density of 30 mA cm^{-2} were performed over 50 h (Fig. 3e). The electrode stability was confirmed in a two-electrode configuration without reference and counter electrodes not only because the possible dissolution/re-deposition of Pt may occur, but also it is the most practical way to evaluate operational stability of catalyst in PV–electrochemical (PV-EC) devices. Although a slight potential increase was observed after 48 h, this deterioration did not originate from the catalyst degradation because the same activity was achieved even after the old electrolyte was replaced by a fresh one (Fig. S11). The chemical states of the surface of Pt^1/MoP/PCC were identified by XPS analysis (Fig. S12). Although the Mo-P bonding appeared presumably due to the slight Pt detachment, there was no significant change in the chemical states after the stability test. In addition, there were no changes in the microstructure and chemical phase of Pt^1/MoP/PCC, as confirmed by the SEM images and XRD patterns after the 50 h stability test (Fig. S13 and S14). It is speculated that the decreasing concentration of SO_3^{2-} in the electrolyte (reaching approximately 78% of the initial value after 24 h operation assuming 100% Faradaic efficiency) can be attributed as the main cause of the potential increase.

The kinetics of the electrochemical oxidation of Na_2SO_3 (aq) was monitored by in-situ pH measurements, and SO_3^{2-}/SO_4^{2-} ions in the electrolyte before and after the SOR were obtained via High-performance liquid chromatography (HPLC). Fig. S15 depicts the variations in the electrolyte pH and the required potential during H_2 production over 22 h (at a constant current density of 30 mA cm^{-2}) when the Pt/PCC electrode was used. During the entire process, the pH barely changed from the initial pH of 12.8. Three initial sulfur species are available in a Na_2SO_3 (aq) solution: sulfite ions (SO_3^{2-}), bisulfite ions (HSO_3^-), and sulfurous acid (H_2SO_3) [11,44]. The concentrations of these three species can be determined by pH-dependent chemical equilibrium calculations [11,44]. The pH of the solution was greater than 10.96; therefore, the aqueous solution contained approximately 100% SO_3^{2-} ions [11]. Therefore, the only possible reaction pathway for the electrochemical oxidation is given by Eqs. (1)–(3). The HPLC analysis of the solutions taken before and after the reaction confirmed that SO_3^{2-} ions are converted into SO_4^{2-} ions within 22 h (Table S4). The oxidation from SO_3^{2-} to SO_4^{2-} did not affect the solution pH variation because no extra protons or hydroxide ions were released during the reaction.

With the highly efficient MoP-based bifunctional catalyst, state-of-the art perovskite–Si tandem solar cells were prepared by stacking perovskite top cells on a Si solar cell using the same method as in a previous work [32]. As shown in Fig. S16a and b, on top of the Si bottom cell, the following layers are deposited: ITO as a recombination layer, PTAA, wide-bandgap perovskite, C_{60}, and PEIE as an electron transport layer (see Experimental section for details). Phenethylammonium iodide (PEAI) and $Pb(SCN)_2$ additives were employed to passivate the defects of the wide-bandgap perovskite phase. The PV parameters of the perovskite–Si tandem PV system are summarized in Table 1. The device showed a maximum *PCE* of 26.60%, short-circuit current density (J_{SC}) of 19.47 mA cm^{-2}, open-circuit voltage (V_{OC}) of 1.78 V, and fill factor (*FF*) of 76.66% with negligible J–V hysteresis.

Table 1
Photovoltaic parameters of perovskite–Si tandem cell.

	V_{oc} (V)	J_{sc} (mA cm^{-2})	*FF* (%)	*PEC* (%)
Forward (J_{sc} to V_{oc})	1.80	19.28	76.12	26.42
average	1.82 ± 0.03	19.12 ± 0.23	74.92 ± 1.19	26.11 ± 0.36
Reverse (V_{oc} to J_{sc})	1.78	19.47	76.66	26.60
average	1.81 ± 0.03	19.26 ± 0.29	75.79 ± 1.97	26.45 ± 0.15

3.3. Unbiased Solar H_2 generating PV–electrochemical device

Combining the tailored efficient bifunctional HER–SOR catalysts and high-efficiency perovskite–Si tandem, an overall PV-EC device was assembled, as schematically shown in Fig. 4a. The perovskite–Si tandem cell was connected with wires to catalyst electrodes immersed in a SO_3^{2-} containing electrolyte and simulated solar irradiation (AM 1.5G) provided the energy to simultaneously produce H_2 and remove SO_3^{2-}. It is important to note that the electrolyte needs to be replenished for efficient H_2 generation, because the SO_3^{2-} in the electrolyte will be depleted. MoP/PCC and Pt^1/MoP/PCC electrodes were utilized as the anode and the cathode, respectively (the resulting electrochemical cell is denoted as MoP ‖ Pt^1/MoP). The active areas of the electrodes and the tandem PV cell were the same. The operating current density of the overall water splitting device was estimated at the intersection of the separately measured J–V curves of the PV cell and the two-electrode electrocatalyst (Fig. 4b). Clearly, the higher required potential for water splitting limited the operating current when the HER was combined with the OER, whereas a remarkably high operating current of approximately 18 mA cm^{-2} was observed when coupled with the SOR. To confirm the actual performance of the standalone PV–electrocatalysis device, we performed J–V curve measurements with a two-electrode configuration, combining the PV with either MoP ‖ Pt^1/MoP (i.e., PV–MoP ‖ Pt^1/MoP). The top and bottom electrodes of the PV were connected to Pt^1/MoP/PCC and MoP/PCC, respectively; therefore, the electrons moved to the surface of Pt^1/MoP/PCC (cathode), whereas the holes were transferred to MoP/PCC (anode). Inset in Fig. 4b shows the J–V curve of the overall electrolysis device. The current value at 0 V represents the unbiased reaction rate in the two-electrode mode. The current density agreed well with the value determined by the intercept of the J–V curves for each device. The measured unbiased solar H_2 production current density for the overall device is 17.23 mA cm^{-2} for *HER+SOR*, whereas it is only 3.92 mA cm^{-2} for *HER+OER*. The slightly lower current density than that predicted presumably results from the series resistance of the cell connections. In addition, H_2 evolution over the Pt^1/MoP/PCC electrode was monitored via GC at the operating point of 1.4 V in a two-electrode configuration. As shown in Fig. S17, the Faradaic efficiency of the HER was calculated as > 90% by comparing the detected and theoretical H_2 amounts, based on the passed charge carriers. It should be emphasized here that no oxygen was generated during this reaction, signifying that gas separation is no longer necessary in our *HER+SOR* system.

A systematic comparison of the H_2 generating current density with previously reported traditional water splitting device in the literature confirms that the present work achieves the highest current density under 1 sun illumination (Fig. 4c and Table S5). This is noteworthy that many of earlier works were mainly relied on noble-metal or III-V semiconductors to overcome high overpotential of water splitting. Therefore, it is suggested that low cost MoP-based catalysts can play an important role in efficient H_2 generation when combined with the SOR instead of the OER. Fig. 4d shows the I–t curve under 1-sun illumination without an additional electrical bias. The system presented long-term operational stability by which the photocurrent remained stable over 50 h of H_2 generation with only a small decline in the current density while delivering approximately 96% of the initial current. Even after 80 h of continuous operation, 70% of the initial current was maintained (Fig. S18a). The degraded current density is attributed to the deterioration of both PV cell and catalytic electrode (Fig. S18b). The PV tandem cell deteriorated, probably owing to the degradation of the perovskite top cell. The decreased *FF* can be ascribed to the decreased shunt resistance of the perovskite top cell. Interestingly, there was no significant change in the XRD patterns for Pt^1/MoP/PCC between samples before and after the 80 h stability test. (Fig. S19a), suggesting that the bulk MoP phase remained during the 80 h stability test. The P/Mo atomic ratio on the Pt^1/MoP/PCC surface was identified by XPS analysis. As shown in Fig. S19b, the ratio of P/Mo decreased, indicating that P atoms are dissolved preferentially over Mo in MoP, which is induced by an alkaline electrolyte [45]. In addition, compared to the initial electrode and that after 50 h of operation (Fig. S13), the sample after 80 h test of Pt^1MoP/PCC electrode presented a different smooth surface morphology, indicating that MoP was dissolved in the electrolyte (Fig. S19c). Therefore, it is speculated that the degradation of electrocatalytic performance of Pt^1MoP/PCC is mainly originated from the surface dissolution, where the electrochemical reaction occurs. By comparing with previous attempts to combine the HER with the SOR, we demonstrated for the first time a stable high current density under an unbiased condition [18,19]. Moreover, this high current density (i.e., H_2 production) corresponds to an exceptionally high solar-to-hydrogen efficiency of 21.2% from a typical *HER+OER* device. The amount of H_2 generated can be calculated from the current density. Assuming 100% Faradaic efficiency, a 1 cm^2-sized bias-free overall PV–electrolysis device can produce approximately 85 mL H_2 from 250 mL of 0.25 M SO_3^{2-}-containing electrolyte for a half day (12 h, 25 °C, 1 atm).

Fig. 5 graphically summarizes the hypothetical integration of solar H_2 generation with SO_2 removal. Even with the strict regulation of SO_2 emissions, 50 million tons of SO_2 gas is still released into the atmosphere, implying that the amount of SO_2 gas produced is much higher, presumably as high as the annual demand for H_2 gas (∼ 70 million tons) [46]. In addition, fossil fuel-based power plants that release SO_2 must be built near accessible water sources because boiling water is necessary for electricity generation. Hence, it is easy to obtain a large amount of the reactant (i.e., SO_3^{2-} and H_2O) from fossil fuel-based power plants, from which H_2 can be sufficiently produced when the SOR is integrated with solar H_2 generation. Although the SOR by-product (i.e., Na_2SO_4) is nontoxic and can be used in various applications, it can also be further converted into valuable products, such as H_2SO_4 and NaOH, by electrodialysis using a heterogeneous bipolar membrane [17]. Therefore, our proposed PV–EC system based on the SOR presents a new sustainable strategy to produce H_2 as well as benefit various industries without an expensive waste treatment of flue gas.

4. Conclusions

Our unbiased H_2-generating PV–EC system uses solar energy to produce H_2 along with waste treatment. By coupling with SOR at the anode, the photoassisted device exhibits an exceptionally high H_2 generation photocurrent density of over 17 mA cm^{-2} under 1-sun illumination as well as sufficient operational stability for 50 h. Replacement of the anodic OER with the SOR allowed reduction in the required potential for H_2 generation, which was supplied by perovskite–Si tandem PV. The development of bi-function MoP-based electrocatalysts for HER and SOR plays an important role in simplifying overall system design and achieving cost-effective H_2 production. The MoP/PCC anode presented superior electrocatalytic performance for the SOR owing to its higher intrinsic catalytic activity, whereas the Pt^1/MoP/PCC cathode exhibited high electrocatalytic activity toward the HER in alkaline medium owing to the synergetic effect of MoP and Pt. By combining perovskite–Si tandem PV with the MoP ‖ Pt^1/MoP electrodes, we demonstrated that the combination of *HER+SOR* is more beneficial than *HER+OER* in terms of the higher reaction rate, reduced cost owing to the elimination of gas separation, and the values of the product. Our proposed strategy paves the way for decarbonizing the current H_2 production while producing value-added products from SO_2 waste.

CRediT authorship contribution statement

Jaemin Park: Conceptualization, Methodology, Validation, Writing – original draft. **Hyunseok Yoon:** Validation, Writing – original draft. **Dong-Yeop Lee:** Methodology, Resources. **Su Geun Ji:** Methodology, Resources. **Wooseok Yang:** Writing – review & editing. **S. David Tilley:** Writing – review & editing. **Myeong-Chang Sung:** Resources. **Ik Jae Park:** Resources. **Jeiwan Tan:** Investigation. **Hyungsoo Lee:**

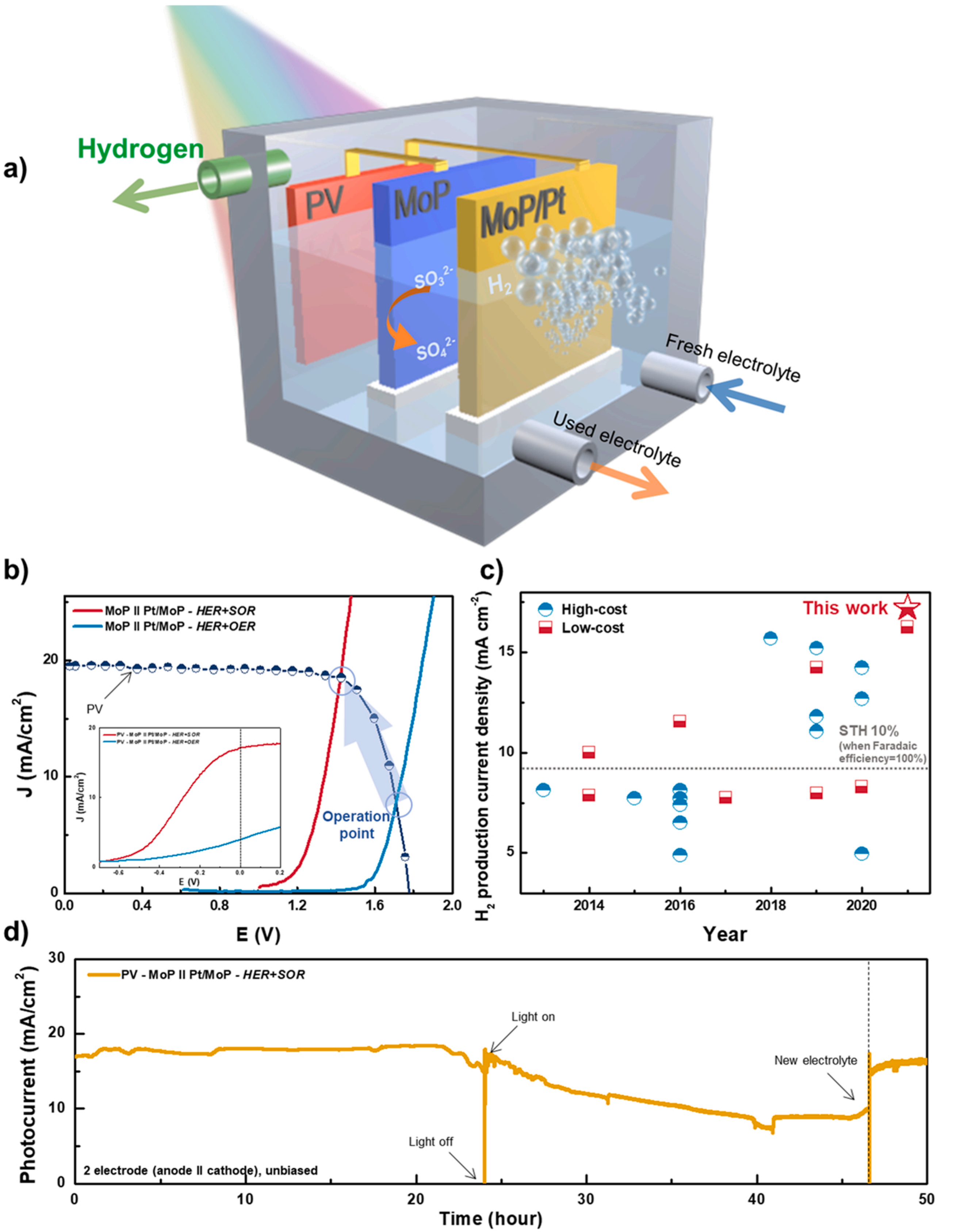

Fig. 4. a) Schematic of water splitting device using SOR. b) J–V curve of tandem PV cell under AM 1.5G illumination and MoP ‖ Pt[1]/MoP with *Na_2SO_3 (0.25)* electrolyte and MoP ‖ Pt[1]/MoP with *NaOH only* electrolyte in two-electrode configuration. Performance of overall device is displayed as an inset. c) Comparison of the H_2 generating current density achieved in this work with the reported values for other solar-driven water splitting systems. d) Unbiased water splitting performance of overall device with PV–MoP ‖ Pt[1]/MoP under AM 1.5G illumination.

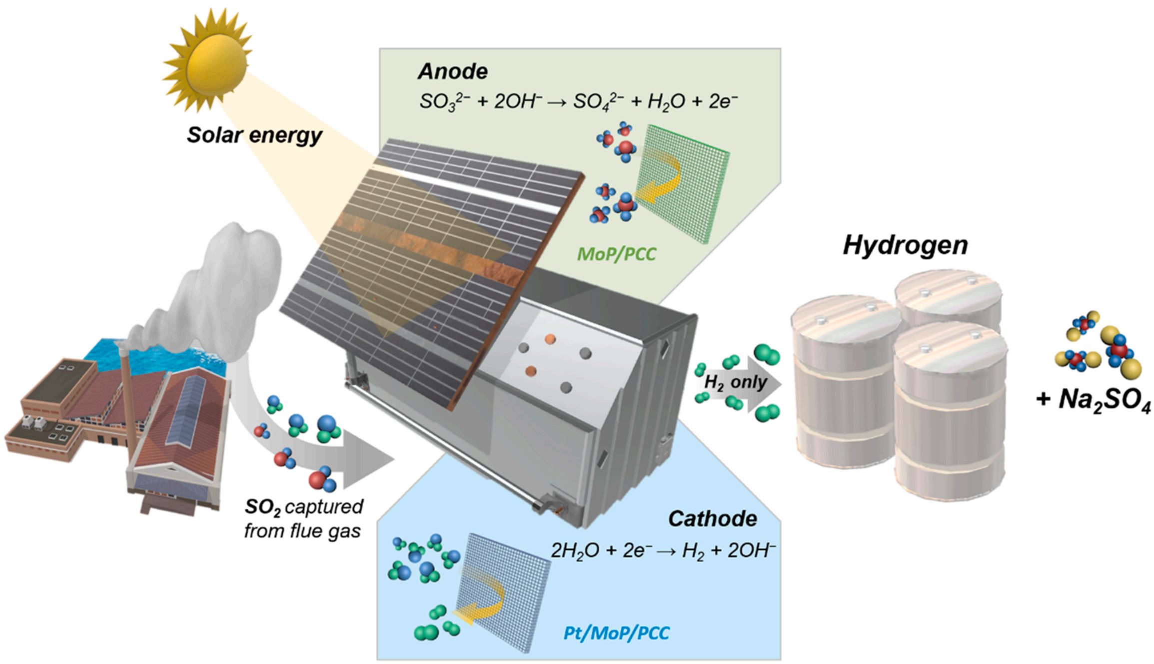

Fig. 5. Schematic of integration of SO_2 removal and solar hydrogen generation by photoassisted water electrolysis system.

Investigation. **Jin Young Kim:** Writing – review & editing. **Dong-Wan Kim:** Writing – review & editing. **Jooho Moon:** Supervision, Writing – review & editing, Funding acquisition.

Declaration of Competing Interest

The authors declare that they have no known competing financial interests or personal relationships that could have appeared to influence the work reported in this paper.

Acknowledgments

This research was supported by National R&D Program through the National Research Foundation of Korea (NRF) funded by Ministry of Science and ICT, Republic of Korea (2021R1A3B1068920, 2021M3H4A1A03049662, and 2021M3D1A2051636). This research was also supported by the Yonsei Signature Research Cluster Program of 2021, Republic of Korea (2021-22-0002).

Appendix A. Supporting information

Supplementary data associated with this article can be found in the online version at doi:10.1016/j.apcatb.2021.121045.

References

[1] B. Liddle, P. Sadorsky, P, How much does increasing non-fossil fuels in electricity generation reduce carbon dioxide emissions, Appl. Energy 197 (2017) 212–221, https://doi.org/10.1016/j.apenergy.2017.04.025.

[2] J.A. de Gouw, D.D. Parrish, G.J. Frost, M, Reduced emissions of CO_2, NO_x, and SO_2 from US power plants owing to switch from coal to natural gas with combined cycle technology, Earths Future 2 (2014) 75–82, https://doi.org/10.1002/2013EF000196.

[3] S.Z. Baykara, Hydrogen: a brief overview on its sources, production and environmental impact, Int. J. Hydrogen Energy 43 (2018) 10605–10614, https://doi.org/10.1016/j.ijhydene.2018.02.022.

[4] N.S. Lewis, Research opportunities to advance solar energy utilization, Science 351 (2016), https://doi.org/10.1126/science.aad1920.

[5] J.S. Luo, J.H. Im, M.T. Mayer, M. Schreier, M.K. Nazeeruddin, N.G. Park, S. D. Tilley, H.J. Fan, M. Gratzel, Water photolysis at 12.3% efficiency via perovskite photovoltaics and Earth-abundant catalysts, Science 345 (2014) 1593–1596, https://doi.org/10.1126/science.1258307.

[6] N.-T. Suen, S.-F. Hung, Q. Quan, N. Zhang, Y.-J. Xu, H.M. Chen, Electrocatalysis for the oxygen evolution reaction: recent development and future perspectives, Chem. Soc. Rev. 46 (2017) 337–365. 〈https://pubs.rsc.org/en/content/articlelanding/2017/cs/c6cs00328a〉.

[7] Y. Goto, T. Hisatomi, Q. Wang, T. Higashi, K. Ishikiriyama, T. Maeda, Y. Sakata, S. Okunaka, H. Tokudome, M. Katayama, S. Akiyama, H. Nishiyama, Y. Inoue, T. Takewaki, T. Setoyama, T. Minegishi, T. Takata, T. Yamada, K. Domen, A particulate photocatalyst water-splitting panel for large-scale solar hydrogen generation, Joule 2 (2018) 509–520, https://doi.org/10.1016/j.joule.2017.12.009.

[8] M.T. Bender, X. Yuan, K.-S. Choi, Alcohol oxidation as alternative anode reactions paired with (photo)electrochemical fuel production reactions, Nat. Commun. 11 (2020) 4594. 〈https://www.nature.com/articles/s41467-020-18461-1〉.

[9] C.R. Lhermitte, K. Sivula, Alternative oxidation reactions for solar-driven fuel production, ACS Catal. 9 (2019) 2007–2017, https://doi.org/10.1021/acscatal.8b04565.

[10] Lu Lu, Waltteri Vakki, Jeffery A. Aguiar, Chuanxiao Xiao, Katherine Hurst, Michael Fairchild, Xi Chen, Fan Yang, Jing Gu, Zhiyong Jason Ren, Unbiased solar H_2 production with current density up to 23 mA cm^{-2} by Swiss-cheese black Si coupled with wastewater bioanode, Energy Environ. Sci. 12 (2019) 1088–1099, https://doi.org/10.1039/C8EE03673J.

[11] C.P. Huang, C.A. Linkous, O. Adebiyi, A. T-Raissi, Hydrogen production via photolytic oxidation of aqueous sodium sulfite solutions, Environ. Sci. Technol. 44 (2010) 5283–5288, https://doi.org/10.1021/es903766w.

[12] J.H. Park, J.W. Ahn, K.H. Kim, Y.S. Son, Historic and futuristic review of electron beam technology for the treatment of SO_2 and NO_x in flue gas, Chem. Eng. J. 355 (2019) 351–366, https://doi.org/10.1016/j.cej.2018.08.103.

[13] L.J. Yang, J.J. Bao, J.P. Yan, J.H. Liu, S.J. Song, F.X. Fan, Removal of fine particles in wet flue gas desulfurization system by heterogeneous condensation, Chem. Eng. J. 156 (2010) 25–32, https://doi.org/10.1016/j.cej.2009.09.026.

[14] S. van Ewijk, W. McDowall, Diffusion of flue gas desulfurization reveals barriers and opportunities for carbon capture and storage, Nat. Commun. 11 (2020) 4298. 〈https://www.nature.com/articles/s41467-020-18107-2〉.

[15] R.K. Srivastava, W. Jozewicz, Flue gas desulfurization: the state of the art, J. Air Waste Manag. 51 (2001) 1676–1688, https://doi.org/10.1080/10473289.2001.10464387.

[16] Y.T. Ma, Q.K. Nie, R. Xiao, W. Hu, B.Y. Han, P.A. Polaczyk, B.S. Huang, Experimental investigation of utilizing waste flue gas desulfurized gypsum as backfill materials, Constr. Build. Mater. 245 (2020), 118393, https://doi.org/10.1016/j.conbuildmat.2020.118393.

[17] J. Kroupa, J. Kinčl, J. Cakl, Desalin. Recovery of H_2SO_4 and NaOH from Na_2SO_4 by electrodialysis with heterogeneous bipolar membrane, Water Treat. 56 (2015) 3238–3246, https://doi.org/10.1080/19443994.2014.980972.

[18] S. Chen, W. Zhou, Y.N. Ding, G.B. Zhao, J.H. Gao, Energy-saving cathodic hydrogen production enabled by anodic oxidation of aqueous sodium sulfite solutions, Energy Fuels 34 (2020) 9058–9063, https://doi.org/10.1021/acs.energyfuels.0c01589.

[19] J. Han, H.Y. Cheng, L.W. Zhang, H.B. Fu, J.M. Chen, Trash to treasure: use flue gas SO_2 to produce H_2 via a photoelectrochemical process, Chem. Eng. J. 335 (2018) 231–235, https://doi.org/10.1016/j.cej.2017.10.116.

[20] P. Xiao, M.A. Sk, L. Thia, X. Ge, R.J. Lim, J.-Y. Wang, K.H. Lim, X. Wang, Molybdenum phosphide as an efficient electrocatalyst for the hydrogen evolution

reaction, Energy Environ. Sci. 7 (2014) 2624–2629, https://doi.org/10.1039/C4EE00957F.
[21] X. Zhang, X. Yu, L. Zhang, F. Zhou, Y. Liang, R. Wang, Molybdenum phosphide/carbon nanotube hybrids as pH-universal electrocatalysts for hydrogen evolution reaction, Adv. Funct. Mater. 28 (2018), 1706523, https://doi.org/10.1002/adfm.201706523.
[22] R. Ge, J. Huo, T. Liao, Y. Liu, M. Zhu, Y. Li, J. Zhang, W. Li, Hierarchical molybdenum phosphide coupled with carbon as a whole pH-range electrocatalyst for hydrogen evolution reaction, Appl. Catal. B 260 (2020), 118196, https://doi.org/10.1016/j.apcatb.2019.118196.
[23] E.J. Popczun, J.R. McKone, C.G. Read, A.J. Biacchi, A.M. Wiltrout, N.S. Lewis, R. E. Schaak, Nanostructured nickel phosphide as an electrocatalyst for the hydrogen evolution reaction, J. Am. Chem. Soc. 135 (2013) 9267–9270, https://doi.org/10.1021/ja403440e.
[24] Y. Men, P. Li, J. Zhou, S. Chen, W. Luo, Trends in alkaline hydrogen evolution activity on cobalt phosphide electrocatalysts doped with transition metals, Cell Rep. Phys. Sci. 1 (2020), 100136, https://doi.org/10.1016/j.xcrp.2020.100136.
[25] Y. Jiao, H. Yan, R. Wang, X. Wang, X. Zhang, A. Wu, C. Tian, B. Jiang, H. Fu, Porous plate-like MoP assembly as an efficient pH-universal hydrogen evolution electrocatalyst, ACS Appl. Mater. Interfaces 12 (2020) 49596–49606, https://doi.org/10.1021/acsami.0c13533.
[26] C. Pi, C. Huang, Y. Yang, H. Song, X. Zhang, Y. Zheng, B. Gao, J. Fu, P.K. Chu, K. Huo, In situ formation of N-doped carbon-coated porous MoP nanowires: a highly efficient electrocatalyst for hydrogen evolution reaction in a wide pH range, Appl. Catal. B 263 (2020), 118358, https://doi.org/10.1016/j.apcatb.2019.118358.
[27] D.-Y. Lee, H.J. Song, D.-W. Kim, Wide pH range electrocatalytic hydrogen evolution using molybdenum phosphide nanoparticles uniformly anchored on porous carbon cloth, Ceram. Int. 47 (2021) 9347–9353, https://doi.org/10.1016/j.ceramint.2020.12.065.
[28] N.T.L. Mai, L.G. Bach, H.T. Nhac-Vu, Q.B. Bui, Hierarchical star-like molybdenum phosphides nanostructures decorated graphene on 3D foam as self-supported electrocatalyst for hydrogen evolution reaction, Solid State Sci. 101 (2020), 106143, https://doi.org/10.1016/j.solidstatesciences.2020.106143.
[29] W. Xiao, L. Zhang, D. Bukhvalov, Z. Chen, Z. Zou, L. Shang, X. Yang, D. Yan, F. Han, T. Zhang, Hierarchical ultrathin carbon encapsulating transition metal doped MoP electrocatalysts for efficient and pH-universal hydrogen evolution reaction, Nano Energy 70 (2020), 104445, https://doi.org/10.1016/j.nanoen.2020.104445.
[30] Y. Teng, X.-D. Wang, H.-Y. Chen, J.-F. Liao, W.-G. Li, D.-B. Kuang, Iron-assisted engineering of molybdenum phosphide nanowires on carbon cloth for efficient hydrogen evolution in a wide pH range, J. Mater. Chem. A 5 (2017) 22790–22796, https://doi.org/10.1039/C7TA07895A.
[31] H.J. Song, M.C. Sung, H. Yoon, B. Ju, D.W. Kim, Ultrafine alpha-phase molybdenum carbide decorated with platinum nanoparticles for efficient hydrogen production in acidic and alkaline media, Adv. Sci. 6 (2019), 1802135, https://doi.org/10.1002/advs.201802135.
[32] D. Kim, H.J. Jung, I.J. Park, B.W. Larson, S.P. Dunfield, C.X. Xiao, J. Kim, J. H. Tong, P. Boonmongkolras, S.G. Ji, F. Zhang, S.R. Pae, M. Kim, S.B. Kang, V. Dravid, J.J. Berry, J.Y. Kim, K. Zhu, D.H. Kim, B. Shin, Efficient, stable silicon tandem cells enabled by anion-engineered wide-bandgap perovskites, Science 368 (2020) 155, https://doi.org/10.1126/science.aba3433.
[33] Y. Zhou, X. Yu, F. Sun, J. Zhang, MoP supported on reduced graphene oxide for high performance electrochemical nitrogen reduction, Dalton Trans. 49 (2020) 988–992, https://doi.org/10.1039/C9DT04441H.
[34] M. Hou, X. Teng, J. Wang, Y. Liu, L. Guo, L. Ji, C. Cheng, Z. Chen, Multiscale porous molybdenum phosphide of honeycomb structure for highly efficient hydrogen evolution, Nanoscale 10 (2018) 14594–14599, https://doi.org/10.1039/C8NR04246B.
[35] Y. Jiang, Y. Lu, J. Lin, X. Wang, Z. Shen, A hierarchical MoP nanoflake array supported on Ni foam: a bifunctional electrocatalyst for overall water splitting, Small Methods 2 (2018), 1700369, https://doi.org/10.1002/smtd.201700369.
[36] L. Zhang, Z. Jin, N. Tsubaki, MoP@MoO_3 S-scheme heterojunction in situ construction with phosphating MoO_3 for high efficient photocatalytic hydrogen production, Nanoscale 13 (2021) 18507, https://doi.org/10.1039/D1NR05452J.
[37] F. Wang, B. Fang, X. Yu, L. Feng, Coupling ultrafine Pt nanocrystals over the Fe_2P Surface as a robust catalyst for alcohol fuel electro-oxidation, ACS Appl. Mater. Interfaces 11 (2019) 9496–9503, https://doi.org/10.1021/acsami.8b18029.
[38] Y. Pei, B. Rezaei, X. Zhang, Z. Li, H. Shen, M. Yang, J. Wang, Interface catalysis by Pt nanocluster@Ni_3N for bifunctional hydrogen evolution and oxygen evolution, Mater. Chem. Front. 4 (2020) 2665–2672, https://doi.org/10.1039/D0QM00326C.
[39] J. Rong, G. Zhu, W. Ryan Osterloh, Y. Fang, Z. Ou, F. Qiu, K.M. Kadish, In situ construction MoS_2-Pt nanosheets on 3D MOF-derived S, N-doped carbon substrate for highly efficient alkaline hydrogen evolution reaction, Chem. Eng. J. 412 (2021), 127556, https://doi.org/10.1016/j.cej.2020.127556.
[40] L. Liao, S.N. Wang, J.J. Xiao, X.J. Bian, Y.H. Zhang, M.D. Scanlon, X.L. Hu, Y. Tang, B.H. Liu, H.H. Girault, A nanoporous molybdenum carbide nanowire as an electrocatalyst for hydrogen evolution reaction, Energy Environ. Sci. 7 (2014) 387–392, https://doi.org/10.1039/C3EE42441C.
[41] C.C.L. McCrory, S.H. Jung, J.C. Peters, T.F. Jaramillo, Benchmarking heterogeneous electrocatalysts for the oxygen evolution reaction, J. Am. Chem. Soc. 135 (2013) 16977–16987, https://doi.org/10.1021/ja407115p.
[42] R. Subbaraman, D. Tripkovic, D. Strmcnik, K.C. Chang, M. Uchimura, A. P. Paulikas, V. Stamenkovic, N.M. Markovic, Enhancing hydrogen evolution activity in water splitting by tailoring Li^+-$Ni(OH)_2$-Pt interfaces, Science 334 (2011) 1256–1260, https://doi.org/10.1126/science.1211934.
[43] P.E.R. Blanchard, A.P. Grosvenor, R.G. Cavell, A. Mar, Effects of metal substitution in transition-metal phosphides (Ni1-xM '(x))(2)P (M ' = Cr, Fe, Co) studied by X-ray photoelectron and absorption spectroscopy, J. Mater. Chem. A 19 (2009) 6015–6022, https://doi.org/10.1039/B904250D.
[44] M. Pourbaix, X.Z. Yang, H.M. Zhang, Z.C. Zhang, Some oxidation equilibria - towards the setting-up of atlases of chemical and electrochemical equilibria in the presence of a gaseous-phase, Corros. Sci. 26 (1986) 873–917, https://doi.org/10.1016/0010-938X(86)90081-8.
[45] I.-S. Kim, H.-S. Cho, M. Kim, H.-J. Oh, S.-Y. Lee, Y.-K. Lee, C. Lee, J.H. Lee, W. C. Cho, S.-K. Kim, J.H. Joo, C.-H. Kim, Sacrificial species approach to designing robust transition metal phosphide cathodes for alkaline water electrolysis in discontinuous operation, J. Mater. Chem. A 9 (2021) 16713–16724, https://doi.org/10.1039/D1TA01181B.
[46] IEA, The Future of Hydrogen. IEA Paris, 2019. ⟨https://www.iea.org/reports/the-future-of-hydrogen⟩.